NANO LETTERS
Letter
Cite This: Nano Lett. XXXX, XXX, XXX−XXX
pubs.acs.org/NanoLett

Barrier Inhomogeneities in Atomic Contacts on WS_2

Krystian Nowakowski,[†] Harold J. W. Zandvliet,[†] and Pantelis Bampoulis*[,†,§]

[†]Physics of Interfaces and Nanomaterials, MESA+ Institute for Nanotechnology, University of Twente, P.O. Box 217, 7500AE Enschede, The Netherlands

[§]Physikalisches Institut, Universität zu Köln, Zülpicher Straße 77, 50937 Köln, Germany

Supporting Information

ABSTRACT: The down-scaling of electrical components requires a proper understanding of the physical mechanisms governing charge transport. Here, we have investigated atomic-scale contacts and their transport characteristics on WS_2 using conductive atomic force microscopy (c-AFM). We demonstrate that c-AFM can provide true atomic resolution, revealing atom vacancies, adatoms, and periodic modulations arising from electronic effects. Moreover, we find a lateral variation of the surface conductivity that arises from the lattice periodicity of WS_2. Three distinct sites are identified, i.e., atop, bridge, and hollow. The current transport across these atomic metal−semiconductor interfaces is understood by considering thermionic emission and Fowler−Nordheim tunnelling. Current modulations arising from point defects and the contact geometry promise a novel route for the direct control of atomic point contacts in diodes and devices.

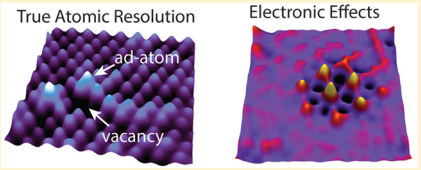

KEYWORDS: *Barrier height, atomic contacts, conductive atomic force microscopy, defects, transition metal dichalcogenides, WS_2*

Perhaps the biggest fundamental issue with down-scaling electronic devices is the miniaturization of the metal−semiconductor (MS) contact to the point where quantum mechanical effects dominate the charge transport. Understanding the charge transport across atomic-scale contacts is therefore crucial in realizing nanodevices. The physics governing atomic point contacts have been addressed by various techniques. These include the break-junction method,[1,2] scanning tunnelling microscopy (STM),[3−6] and theoretical calculations.[7−10] Several physical phenomena have been observed, including the quantization of conductance,[1,5] atom manipulation,[11] Kondo interactions,[12,13] and the formation of ultra-small Schottky diodes.[14,15]

The lateral variation in the atomic lattice of a surface causes significant variations in the conductance.[7−9,16,17] Evidence of this atomic-scale variation of conductance comes from STM and c-AFM studies operated in atomic contact with the surface.[16,18,19] In these studies, the actual contact often involves several tip atoms, as it is evident from the absence of real atomic resolution (inability to measure defects such as vacancies and adatoms). The observed atomic periodicity is the result of tip convolution and bears some similarities with the atomic periodicity obtained in lateral force microscopy (LFM).[20]

In the case of a MS contact, a Schottky barrier (SB) is often formed. For macroscopic contacts, the thermionic emission (TE) model describes adequately the charge transport across the SB formed at the interface.[21] However, for nanoscopic MS junctions, deviations from the above model have been frequently observed in both c-AFM and STM studies.[22−25] These deviations point to the inapplicability of the model derived for an infinite MS interface to the contact of a nanoscopic size.[21,24,25] Given the importance of nano-Schottky contacts to nanodevices, there have been substantial efforts to understand the involved physical mechanisms.[15,23,24] Smit et al.[24,25] predicted that the ratio of tunnelling to TE at the MS interface increases with decreasing the contact size, due to the reduction of the SB width. Indeed, often the electron injection from the metallic tip into the semiconductor via Fowler−Nordheim (F−N) tunnelling is so effective that the polarity of the junction seems to be switched, i.e., the current is actually higher in the TE reverse bias regime.[26]

Here, we have used c-AFM to investigate the surface conductivity of WS_2 down to the atomic level. WS_2 belongs to transition metal dichalcogenides (TMDC), a group of materials that has recently attracted a lot of attention due to their thickness-dependent electronic properties[27−29] and their exotic spin-valley-coupled electronic structure.[30−33] We demonstrate that c-AFM can provide true atomic resolution on atomically smooth semiconductor surfaces, such as WS_2, by utilizing quantum point contact microscopy. A pair of imaging modes were identified based on the condition of the tip; a sharp but partially insulating tip and a fully conductive tip. True atomic resolution was only obtained in the former case. Moreover, spatially resolved $I(V)$ characteristics of atomic contacts between the WS_2 surface and the conductive AFM tip reveal a rectifying behavior that can be explained by considering both TE and F−N tunnelling. In addition, the $I(V)$ characteristics display a spatial modulation arising from the underlying lattice periodicity and the distinct atomic contact geometries.

Atomic-Resolution Imaging. It has been shown that c-AFM and quantum point contact microscopy are able to

Received: November 16, 2018
Revised: December 20, 2018
Published: December 24, 2018

DOI: 10.1021/acs.nanolett.8b04636
Nano Lett. XXXX, XXX, XXX−XXX

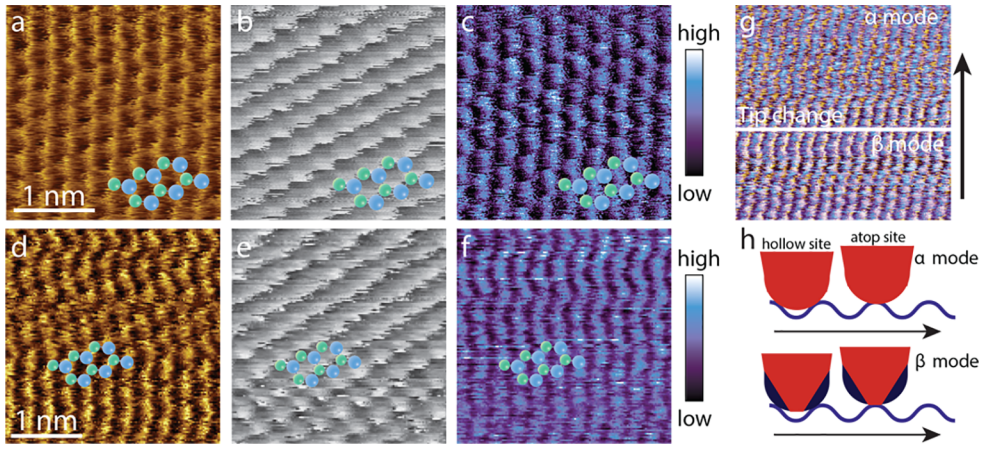

Figure 1. (a) Topography, (b) LFM and (c) current images obtained in mode α with an overdrawn atomic configuration of WS_2 surface (blue denotes S and green W). (d) Topography, (e) LFM, and (f) current images obtained in mode β on the same surface. (g) Overlaid height (gold) and current (blue) signals showing a transition from mode β to mode α, captured in one scan. (h) Schematics of the contact geometry for the two tip configurations as they scan the surface. Red indicates conductive parts and dark blue insulating; note that the representation is out of scale. The current images were recorded with a sample bias of −1 V.

capture the lattice periodicity[34,35] of the surface as well as to give material contrast by identifying, for instance, surface alloys.[18,36] In addition, atomic resolution can be achieved in c-AFM by reducing the contact size of the tip with the surface.[19] So far, single atom vacancies and adatoms have not been visualized. In the following, we demonstrate that it is possible to measure single atom vacancies as well as adatoms in c-AFM.

We start our investigation by looking at two distinct cases, which, at first glance, appear to be identical. The first case is presented in Figure 1a−c, which shows, respectively, the topography, lateral force and current images recorded simultaneously on a freshly cleaved WS_2 surface. In the topography the S atoms form a triangular network characteristic of WS_2, with a lattice constant of 0.32 ± 0.01 nm. The lateral force image reveals a periodic pattern arising from the stick and slip motion of the tip.[20] From these two images, it is clear that the stick is located at the center of each hexagon of the WS_2 lattice. Minima in the lateral force appear at locations assigned to W atoms. The corresponding current image (Figure 1c) reveals that the middle of the cell gives the highest current signal. A different behavior is seen in the second case. Similar to Figure 1a,b, Figure 1d,e shows the same relation between the WS_2 lattice in the topography image and the stick and slip motion in the friction signal. In contrast, in the second case, the current maxima (Figure 1f) come from the S atoms. We note that the two images have been recorded at the same location and only a few minutes apart from each other. The discrepancy in the two images is attributed to different tip configurations; for simplicity, we refer to the first tip configuration as mode α and to the second as mode β.

A tip transition between the two configurations is captured within one scan. In Figure 1g, the simultaneously recorded topography and current signals are overlaid on top of each other. Gold indicates high topography, and blue indicates high current signal. In the lower part of the image, current and topography are in phase with each other (mode β). The current maxima are observed on top of the S atoms. At about half of the image, a tip transition is observed, after which the current maxima are out of phase with the S atoms seen in topography (mode α). Now, the highest currents are obtained at the center of the WS_2 honeycomb. In the case in which the current maxima arise at the centers of the honeycomb, the tip scans the surface in mode α. The current signal is modulated by the surface periodicity, and it is further convoluted by the shape of the tip. When the tip is in a hollow site (middle of the honeycomb), the current increases due to contacting several atoms at once. At the S atom locations, we are dealing with an atomic point contact, and thus, the current is lower than at the hollow sites; see the schematic of Figure 1h (top panel). It is the most common way of measuring in c-AFM and can account for most of the observations in the literature.

Inversion of the current signal in the second case (mode β) is the result of a tip change, which was recorded during scanning (Figure 1g). The shift of the current maxima can be understood by considering differences between the real contact area and the effective electrical contact area.[34] Celano et al.[37] found that often only a small fraction of the physical tip−surface contact area contributes to the current transport. This is not a surprise for conductive AFM tips because exposure to air could lead to a partial oxidation or contamination of the tip. Therefore, considering that the same effect takes place here and the physical contact is larger than the electrical contact, we deduce that the signal in β mode (Figure 1f) is the result of a different mechanism than in α mode (Figure 1c). Indeed, the calculated physical contact area is 0.45 ± 0.15 nm^2, while from adatom imaging, the estimated conductive area is smaller than 0.2 nm^2 (see the Supporting Information). Having an effective electrical contact area smaller than the physical contact area leads to an additional tunnelling barrier at the hollow sites, as shown in the bottom panel of Figure 1h. A barrier arises due to the extra separation between the conductive part of the tip and the surface atoms. This decreases the measured currents at the hollow sites, whereas at the atop sites the conductive part of the tip is still in atomic point contact with the S atoms, which now give higher currents. Similar contrast reversal has been observed in STM imaging when moving from tunneling to contact.[16] Under the scanning conditions used here (force of ∼2−2.5 nN and bias voltage between −1.7 and −0.5 V), the imaging is not destructive (for more information, see the Supporting Information).

Atomic Defects and Electronic Effects. Strikingly, when operating in the β mode, we often find regions with several

DOI: 10.1021/acs.nanolett.8b04636
Nano Lett. XXXX, XXX, XXX−XXX

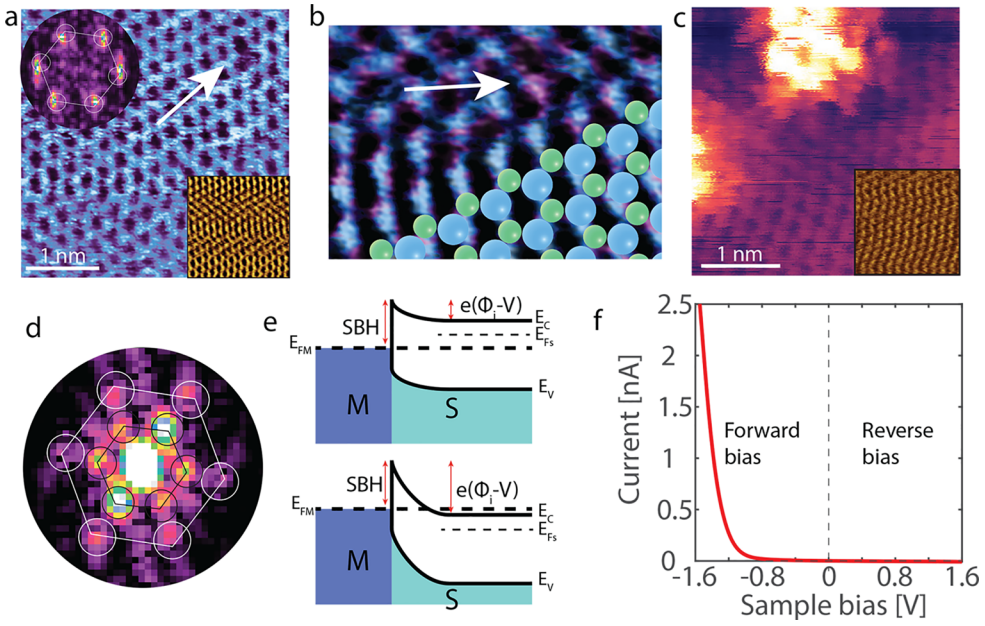

Figure 2. (a) Current image of WS_2 surface showing a chalcogen vacancy (indicated by the arrow). Inset bottom: simultaneously recorded topography image, where the defect is not visible. Inset top: the corresponding FFT revealing the lattice periodicity. (b) An overlay of the topography and current images zoomed on the defect of panel a. Blue indicates a good match between the high values of current and height in the two images, and black indicates a good match between the low current and low height values (hollows). The appearance of purple is due to the bad match between the two signals, indicating a S vacancy. The cartoon at the bottom part of the image presents the WS_2 structure, where blue indicates S atoms and green indicates W atoms (a layer lower). (c) Current image containing other type of surface defects having a large electronic influence in their surroundings. Inset: the simultaneously recorded, defect-less topography image. (d) FFT of panel c. A pair of hexagonal patterns are apparent. The larger hexagon corresponds to the lattice periodicity. The smaller hexagon corresponds to a $\sqrt{3}$ pattern induced by the defects. (e) A simple cartoon of the MS interface when the sample is biased negatively (top) and positively (bottom). (f) $I(V)$ curve recorded on the WS_2 surface, showing a diode-like behavior.

atomic defects on the surface. An example is shown in Figure 2. Figure 2a shows an atomically resolved c-AFM image of the WS_2 surface with a chalcogen defect, indicated with the white arrow. This becomes clear when looking at the overlay of the topography (inset of Figure 2a) and current images shown in Figure 2b. The peaks in the current image align well with the S atoms of the topography image (larger height), giving the blue lattice of Figure 2b. At the location of the defect, the current signal is interrupted, while the topographic signal runs uninterrupted. The purple spot (indicated by the arrow) arises only from the high topography signal at this location, which corresponds to a S atom of the upper layer. The absence of any current signal at this S site indicates that this defect is a S vacancy. The FFT, inset of Figure 2a, reveals a hexagonal symmetry with a period of ~0.32 nm. Often, next to these defects, there is a signature of adatoms in the current image, corresponding to S atoms or O substitution[38] (see the Supporting Information). In contrast to the well-resolved atomic vacancies and adatoms in the current image, the topography image shows a defect-free surface (inset of Figure 2a and the Supporting Information). This striking difference suggests different operating mechanisms between topography and current imaging, in line with the consideration of an electrical contact area smaller than the physical contact area. It also shows that it is possible to obtain true atomic resolution in c-AFM only when the electrically conductive part of the tip is smaller than the tip itself. The missing atoms and adatoms are not current or tip artifacts because they could be imaged with different sample biases and imaging conditions at several different regions on the surface and with different AFM systems (see the Supporting Information).

In addition to atom vacancies, we were also able to image, with c-AFM, intriguing electronic effects arising from point defects, an example of which is shown in Figure 2c. The pattern seen in Figure 2c does not appear in the simultaneously recorded topography, strongly suggesting that it is of purely electronic nature arising from point defects, which as we show earlier, cannot be captured in the topography. Moreover, this pattern is clearly absent around vacancies or adatoms; see Figure 2a,b and the Supporting Information. Therefore, we ascribe the structure seen in Figure 2c to be induced by either defects in the W layer (substitutionals or anti-sites[39,40]) or O defects in the S layer. To understand better this electronic pattern, we have calculated the FFT of Figure 2c and presented it in Figure 2d. It shows the periodicity of the surface (outer hexagonal ring) and a periodicity arising from the electronic pattern at the top part of the image (inner hexagonal ring). Its periodicity amounts to $\sqrt{3}$ times the lattice constant of the surface. The pattern shares some similarities with structures arising from intervalley Q−Q scattering at point defects on WSe_2[41,42] and electronic perturbation caused in the surrounding lattice by oxygen substitution of a S atom on WS_2 and $MoSe_2$.[43] In the former case, the $\sqrt{3}$ pattern observed on WSe_2[41,42] was attributed to intervalley Q−Q scattering in the conduction band (CB), with a wave vector near the M point of the Brillouin zone.[41,24,44,45] The authors observed that the FFT, calculated from scanning tunneling spectroscopy (STS) images, is dominated by scattering associated with the Q valleys.[41,42] This is because the Q valley in the CB of WSe_2 exhibits a spin splitting of ~0.2 eV, i.e., a few times larger than the spin splitting of the K valley, and is lower in energy than

DOI: 10.1021/acs.nanolett.8b04636
Nano Lett. XXXX, XXX, XXX−XXX

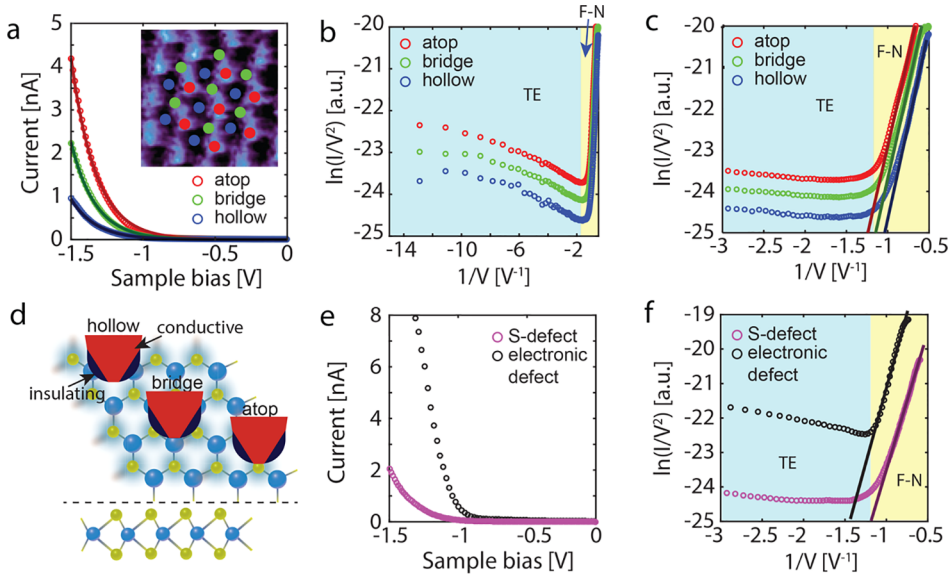

Figure 3. (a) $I(V)$ curves averaged over several single-point curves recorded on atop, bridge, and hollow sites. Inset: c-AFM image with atomic resolution, indicating the atop (red), bridge (green), and hollow (blue) sites (sample bias −1 V). The solid lines show the best fit to TE (eq 1). (b) The same data as in panel a in a Fowler−Nordheim plot: $\ln(I/V^2)$ vs $(1/V)$, showing the Fowler−Nordheim region and TE region. The best fit of the Fowler−Nordheim eq (eq 2) for each of the curves is shown in panel c. (d) Top: schematic drawing of the tip−surface configurations for atop, hollow, and bridge sites. Yellow and blue spheres represent S and W atoms, respectively. The red parts of the tip are conductive, while the dark blue are insulating. Bottom: side view of the WS_2 lattice. (e) $I(V)$ curves recorded on a S vacancy (purple) and an electronic defect (black). (f) The same data as in panel e plotted in a Fowler−Nordheim plot, $\ln(I/V^2)$ vs $(1/V)$, showing the Fowler−Nordheim and TE regions as well as the best fit of eq 2 to the data.

the K valley. The similarity of WS_2 and WSe_2 band structures (Q valley lower than K valley and with a larger spin splitting in the Q valley of the CB)[46,47] along with the good match of the FFT in Figure 2d with the FFTs on WSe_2[41] suggests that the above mechanism could very well account for the observed electronic pattern in Figure 2c.

In the second case, modification of the local density of states (DOS) induced by substitution of S with O leads also to a similar 3-fold symmetry pattern and should not be neglected.[43] Unfortunately, the exact mechanism leading to the obtained $\sqrt{3}$ electronic structure cannot be identified with certainty. Nevertheless, surface defects can unambiguously alter the contact properties in atomic contacts, revealing an additional degree of freedom in the realization of future nanodevices. In addition, the observation of purely electronic defects with c-AFM (at room temperature and N_2 environment) opens the door for new possibilities in characterizing nanodevices in situ and operando.

Here we would like to note that, in contrast to STS, c-AFM does not directly probe the DOS of the surface. In a conventional picture, when an n-type semiconductor is brought in contact with a metal, an n-type SB is expected to form; see Figure 2e. When the semiconductor is negatively biased (forward bias regime), electrons will flow due to TE from the minimum of the conduction band of the semiconductor to the metal; see Figure 2e. This indicates that the observed electronic pattern involves the electrons of the conduction band. Figure 2f shows the $I(V)$ curve averaged over hundreds of single-point curves. The $I(V)$ curve reveals a rectifying Schottky diode behavior, which indicates the formation of a SB in the atomic-scale MS junction. The rectifying properties of the contact do not allow us to investigate possible electronic effects at the positive sample bias. Nevertheless, these measurements demonstrate the extraordinary capabilities of c-AFM, which is able to resolve not only atomic defects but also electronic effects around point defects otherwise only visible with STM and in UHV.[41,42]

Charge-Transport Mechanism. We will now expand our analysis to understand the charge transport in these atomic point contacts in detail. While scanning the surface, we can simultaneously record $I(V)$ traces. We are therefore able to exploit c-AFM to such a level and obtain $I(V)$ characteristics of the atomic junctions. We expect the main transport mechanisms in these atomic scale junctions to involve TE and tunnelling across the SB.[24,25] The current due to the TE is given by:

$$I = AA^*T^2 \exp\left(-\frac{q\Phi_B}{k_B T}\right)\left[\exp\left(\frac{qV}{nk_B T}\right) - 1\right] \quad (1)$$

where q is the elementary charge, V is the bias voltage, k_B is the Boltzmann constant, T is the temperature, n is the ideality factor, A is the electrical contact area, A^* is the Richardson constant ($A^* = 4\pi q m k_B^2 h^{-3}$), Φ_B is the Schottky barrier height (SBH), m is the electron mass, and h is the Planck constant. In this ideal case, in the forward bias regime (negative sample bias for n-type semiconductor), the current increases exponentially with increasing voltage. In the reverse bias regime, the barrier blocks the electrons going from the metal to the semiconductor, and thus, the current saturates. As mentioned in the introductory information, for nanoscale Schottky contacts, the finite-size effects often cause deviations from the ideal case.[24,25,48]

We note that while the tip scans the surface in β mode, the contact with the surface atoms varies precisely and in line with the lattice periodicity of the surface. These contacts can be categorized as atop (over S atom), bridge (over W atom), and hollow sites (the center of the honeycomb) in the lattice of

DOI: 10.1021/acs.nanolett.8b04636
Nano Lett. XXXX, XXX, XXX−XXX

WS_2, as indicated in Figure 3a. The averaged $I(V)$ curves taken at the atop, bridge, and hollow sites are shown in Figure 3a. The three curves differ from each other, providing the observed contrast in the current images. To estimate the SBH at zero bias and the ideality factor, we first assume that the charge transport is mainly due to TE. The fit of the TE model to the recorded curves is shown in Figure 3a. The best fit is obtained for barrier heights equal to 0.17 ± 0.01 eV at atop sites, 0.18 ± 0.01 eV at bridge sites, and 0.19 ± 0.01 eV at hollow sites and ideality factors of 7.0 ± 0.5. The large ideality factor, however, suggests that TE does not describe the data well over the full voltage window. The charge transport is dominated by tunnelling effects, similar to the observations made in previous works.[14,15,23]

As the contact size of the metal−semiconductor junction gets smaller, the tunneling contribution gets larger and eventually takes over as the main charge-carrier injection mechanism.[24,25] There are two possible ways for electrons to tunnel through an energy barrier: direct tunneling or F−N tunneling. From the functional shape of the obtained curves that significantly deviates from a typical direct tunneling $I(V)$ curve (recorded with scanning tunneling spectroscopy), we neglect contributions from direct tunnelling (see the Supporting Information). The current across the junction due to F−N tunnelling is given by:

$$I = \frac{Aq^3mV^2}{8\pi h\Phi_B d^2 m^*} \exp\left[\frac{-8\pi\sqrt{2m^*}\,\Phi_B^{3/2} d}{3hqV}\right] \quad (2)$$

where m^* is the effective mass and d is the barrier width. To evaluate the applicability of F−N tunneling to describe the obtained $I(V)$ curves, we have plotted the data in a F−N plot, i.e., $\ln(I/V^2)$ versus $1/V$. Figure 3b shows the $\ln(I/V^2)$ versus $1/V$ curves recorded at the atop, hollow and bridge sites. The plots show two characteristic regions; at high voltages (low $1/V$), the $\ln(I/V^2)$ depends linearly on $1/V$; at lower voltages (high $1/V$), after a minimum is reached, there is a slow increase of the $\ln(I/V^2)$ values. Figure 3c shows the fit of the F−N equation to the experimental data in the three distinct configurations (atop, hollow, and bridge). At high voltages, F−N tunneling describes well the obtained data. F−N tunneling is the major mechanism at high voltages, where the barrier thickness reduces with voltage. At low voltages (below 0.8 V), the barrier is rather large, F−N tunneling is suppressed, and TE takes over as the main transport mechanism. The qualitative shape of the obtained curves is similar in all three sites. However, in both injection mechanisms the SB determines the current across the interface. Changes in the barrier height and width due to the different contact configurations should have a significant impact on the obtained currents.

By fitting the experimentally obtained $I(V)$ characteristics with eq 2, we can extract the Schottky barrier parameter ($d\Phi_B^{3/2}$). We find that the Schottky barrier parameter significantly differs between the three sites. The Schottky barrier parameter amounts to 1.27 ± 0.01, 1.34 ± 0.01, and 1.36 ± 0.01 $eV^{3/2}$ nm for atop, bridge and hollow sites, respectively. We ascribe the differences in the measured Schottky barrier parameter to differences in the geometry of the tip−surface point contact. The three distinct locations studied here correspond to different tip-contact geometries, as illustrated in Figure 3d. As we described earlier, the electrical contact area is substantially smaller than the physical area (see also the Supporting Information). The electrically conductive part of the tip is assumed to be at the center of the physical contact. At atop sites, the conductive part of the tip is in real contact only with the outermost S atoms. For bridge and hollow sites, small gaps are formed between the electrically conductive part of the tip and the surface atoms, as shown in Figure 1h. These small gaps lead to the formation of tunnelling barriers, increasing further the resistance at these locations and limiting the measured current. In the case of bridge sites, the presence of the W atoms sitting 1.5 Å lower can account for the differences with the hollow sites. Therefore, we conclude that the atomic contacts on semiconductor surfaces, such as WS_2, are sensitive to the exact underlying atom configuration.

It is also of interest to explore the influence of defects on the charge transport characteristics across these atomic contacts. We have looked at the two commonly found defects on our WS_2 samples, namely the S vacancies (e.g., Figure 2a) and the electronic defects (e.g., Figure 2c). I(V) traces recorded on a S vacancy and on an electronic defect are shown in Figure 3e. While the I(V) curve of the S vacancy shows similar behavior as the pristine WS_2 lattice, the electronic defect gives much higher current (as evident also from the c-AFM images). The F−N plots of the two curves are given in Figure 3f, and fitting the curves with eq 2 at the higher voltage range (lower $1/V$) provides a barrier parameter of 1.52 ± 0.01 $eV^{3/2}$nm for the S vacancy and 2.0 ± 0.2 $eV^{3/2}$nm for the electronic defect (the larger spread comes from comparing curves obtained at several different electronic defects). While the current across the S vacancies is dominated by F−N tunneling (similar to the lattice sites of WS_2), at the electronic defects, the current at low voltages is much higher, indicating a larger contribution of TE. This can be understood by a lowering of the barrier height induced by an increase of the local DOS at these locations. Even though this change of the barrier parameter is currently rather unintentional, under the right growth conditions, it can provide an additional degree of freedom in controlling the charge transport at nano and atomic contacts.

Conclusions. The exact transport characteristics of the atomic scale contacts depend on the contact site geometry. This indicates the importance of controlling precisely the interface atomic arrangement of future atomic-size diodes. The rectifying behavior of the atomic point contacts shows a strong promise in their use as active components in nanodevices, e.g., as atomic-scale Schottky diodes. Moreover, we have established c-AFM as an important tool in measuring surfaces with true atomic resolution, obtaining spatially resolved information regarding their conductivity and the involved charge transport mechanisms as well as patterns arising from local modifications in the electronic structure of WS_2. We have also shown that defects on the WS_2 provide an additional degree of freedom in controlling and altering the charge transport at the metal−semiconductor interface. This suggests that direct control of the nature and density of defects will ultimately allow the functionalization and engineering of unique semiconducting nanodevices. The novel use of c-AFM in measuring and visualizing such processes provides new opportunities for material and device characterization.

Methods. The experiments were done with an Agilent 5100 AFM (Agilent) and a Cypher ES AFM (Asylum Research) in contact mode using highly conductive p-type doped diamond tips (spring constant of 0.5 N/m and radius of

DOI: 10.1021/acs.nanolett.8b04636
Nano Lett. XXXX, XXX, XXX−XXX

curvature below 5 nm, AD-E-0.5-SS; Adama Innovations Ltd.). We refer to this probe for simplicity as metallic due to their high electrical conductivity (resistivity of 10^{-5} Ωm). The work function of the used probes has been calibrated with Kelvin probe force microscopy to be around 5 eV. The use of a diamond tip is beneficial because of its high stiffness, stability, and electrical conductivity that allows for stable c-AFM imaging. The force used during scanning was in the order of 2−3 nN, and the radius of the physical contact radius was found using the DMT extension of the Hertz model to be 0.35 ± 0.05 nm[26,49−52] (see the Supporting Informationl). The experiments were done in a N_2 environment (0.1% RH) to avoid water contamination.[53] For the conductive measurements, a bias voltage is applied to the sample (bulk WS_2 and HQ graphene) while the tip is grounded. The electrical connection is completed with silver paint as the second electrode (resistance of a few kΩ). For further details on the experimental setup, see ref 48.

■ ASSOCIATED CONTENT

Supporting Information

The Supporting Information is available free of charge on the ACS Publications website at DOI: 10.1021/acs.nanolett.8b04636.

Additional details on tip shape and contact area, electronic influence of defects, imaging of chalcogen defects, Schottky barrier height mapping, and tunneling spectroscopy (PDF)

■ AUTHOR INFORMATION

Corresponding Author

*E-mail: bampoulis@ph2.uni-koeln.de.

ORCID

Pantelis Bampoulis: 0000-0002-2347-5223

Notes

The authors declare no competing financial interest.

■ ACKNOWLEDGMENTS

We thank The Netherlands Organisation for Scientific Research, NWO (FOM, FV157 14TWDO07) for financial support.

■ REFERENCES

(1) Krans, J. M.; van Ruitenbeek, J. M.; Fisun, V. V.; Yanson, I. K.; de Jongh, L. J. The Signature of Conductance Quantization in Metallic Point Contacts. *Nature* **1995**, *375*, 767−769.

(2) Agraït, N.; Yeyati, A. L.; van Ruitenbeek, J. M. Quantum Properties of Atomic-Sized Conductors. *Phys. Rep.* **2003**, *377*, 81−279.

(3) Gimzewski, J. K.; Möller, R. Transition from the Tunneling Regime to Point Contact Studied Using Scanning Tunneling Microscopy. *Phys. Rev. B: Condens. Matter Mater. Phys.* **1987**, *36*, 1284−1287.

(4) Lang, N. D. Resistance of a One-Atom Contact in the Scanning Tunneling Microscope. *Phys. Rev. B: Condens. Matter Mater. Phys.* **1987**, *36*, 8173−8176.

(5) Olesen, L.; Laegsgaard, E.; Stensgaard, I.; Besenbacher, F.; Schiotz, J.; Stoltze, P.; Jacobsen, K. W.; Norskov, J. K. Quantized Conductance in an Atom-Sized Point Contact. *Phys. Rev. Lett.* **1994**, *72*, 2251−2254.

(6) Becker, M.; Berndt, R. Conductance of Atom-Sized Pb Contacts. *New J. Phys.* **2010**, *12*, 113010.

(7) Hofer, W. A.; Fisher, A. J.; Wolkow, R. A.; Grütter, P. Surface Relaxations, Current Enhancements, and Absolute Distances in High Resolution Scanning Tunneling Microscopy. *Phys. Rev. Lett.* **2001**, *87*, 236104.

(8) Blanco, J. M.; González, C.; Jelínek, P.; Ortega, J.; Flores, F.; Pérez, R. First-Principles Simulations of STM Images: From Tunneling to the Contact Regime. *Phys. Rev. B: Condens. Matter Mater. Phys.* **2004**, *70*, No. 085405.

(9) Makk, P.; Visontai, D.; Oroszlány, L.; Manrique, D. Z.; Csonka, S.; Cserti, J.; Lambert, C.; Halbritter, A. Advanced Simulation of Conductance Histograms Validated through Channel-Sensitive Experiments on Indium Nanojunctions. *Phys. Rev. Lett.* **2011**, *107*, 276801.

(10) Ternes, M.; González, C.; Lutz, C. P.; Hapala, P.; Giessibl, F. J.; Jelínek, P.; Heinrich, A. J. Interplay of Conductance, Force, and Structural Change in Metallic Point Contacts. *Phys. Rev. Lett.* **2011**, *106*, No. 016802.

(11) Limot, L.; Kröger, J.; Berndt, R.; Garcia-Lekue, A.; Hofer, W. A. Atom Transfer and Single-Adatom Contacts. *Phys. Rev. Lett.* **2005**, *94*, 126102.

(12) Néel, N.; Kröger, J.; Limot, L.; Palotas, K.; Hofer, W. A.; Berndt, R. Conductance and Kondo Effect in a Controlled Single-Atom Contact. *Phys. Rev. Lett.* **2007**, *98*, No. 016801.

(13) Choi, D.-J.; Rastei, M. V.; Simon, P.; Limot, L. Conductance-Driven Change of the Kondo Effect in a Single Cobalt Atom. *Phys. Rev. Lett.* **2012**, *108*, 266803.

(14) Svensson, J.; Campbell, E. E. B. Schottky Barriers in Carbon Nanotube-Metal Contacts. *J. Appl. Phys.* **2011**, *110*, 111101.

(15) Wawrzyniak, M.; Michalak, S.; Tomaszewski, D.; Martinek, J. Influence of Schottky Barrier on Conductance of a Metal-Semiconductor Atomic Quantum Point Contact. *Appl. Phys. Lett.* **2016**, *108*, 043104.

(16) Kim, H.; Hasegawa, Y. Site-Dependent Evolution of Electrical Conductance from Tunneling to Atomic Point Contact. *Phys. Rev. Lett.* **2015**, *114*, 206801.

(17) Ondráček, M.; González, C.; Jelínek, P. Reversal of Atomic Contrast in Scanning Probe Microscopy on (111) Metal Surfaces. *J. Phys.: Condens. Matter* **2012**, *24*, No. 084003.

(18) Zhang, Y.-H.; Wahl, P.; Kern, K. Quantum Point Contact Microscopy. *Nano Lett.* **2011**, *11*, 3838−3843.

(19) Rodenbücher, C.; Bihlmayer, G.; Speier, W.; Kubacki, J.; Wojtyniak, M.; Rogala, M.; Wrana, D.; Krok, F.; Szot, K. Local Surface Conductivity of Transition Metal Oxides Mapped with True Atomic Resolution. *Nanoscale* **2018**, *10*, 11498−11505.

(20) Carpick, R. W.; Salmeron, M. Scratching the Surface: Fundamental Investigations of Tribology with Atomic Force Microscopy. *Chem. Rev.* **1997**, *97*, 1163−1194.

(21) Tung, R. T. The Physics and Chemistry of the Schottky Barrier Height. *Appl. Phys. Rev.* **2014**, *1*, 011304.

(22) Pérez-García, B.; Zúñiga-Pérez, J.; Muñoz-Sanjosé, V.; Colchero, J.; Palacios-Lidón, E. Formation and Rupture of Schottky Nanocontacts on ZnO Nanocolumns. *Nano Lett.* **2007**, *7*, 1505−1511.

(23) Kraya, R. A.; Kraya, L. Y. The Role of Contact Size on the Formation of Schottky Barriers and Ohmic Contacts at Nanoscale Metal-Semiconductor Interfaces. *Appl. Phys. Lett.* **2014**, *064302*, 2010−2014.

(24) Smit, G. D. J.; Rogge, S.; Klapwijk, T. M. Scaling of Nano-Schottky-Diodes. *Appl. Phys. Lett.* **2002**, *81*, 3852−3854.

(25) Smit, G. D. J.; Rogge, S.; Klapwijk, T. M. Enhanced Tunneling Across Nanometer-Scale Metal − Semiconductor Interfaces. *Appl. Phys. Lett.* **2002**, *80*, 2568−2570.

(26) Son, Y.; Wang, Q. H.; Paulson, J. A.; Shih, C.-J.; Rajan, A. G.; Tvrdy, K.; Kim, S.; Alfeeli, B.; Braatz, R. D.; Strano, M. S. Layer Number Dependence of MoS2 Photoconductivity Using Photocurrent Spectral Atomic Force Microscopic Imaging. *ACS Nano* **2015**, *9*, 2843−2855.

(27) Choi, W.; Choudhary, N.; Han, G. H.; Park, J.; Akinwande, D.; Lee, Y. H. Recent Development of Two-Dimensional Transition

DOI: 10.1021/acs.nanolett.8b04636
Nano Lett. XXXX, XXX, XXX−XXX

Metal Dichalcogenides and Their Applications. *Mater. Today* **2017**, *20*, 116−130.
(28) Bhimanapati, G. R.; Lin, Z.; Meunier, V.; Jung, Y.; Cha, J.; Das, S.; Xiao, D.; Son, Y.; Strano, M. S.; Cooper, V. R. e. a. Recent Advances in Two-Dimensional Materials beyond Graphene. *ACS Nano* **2015**, *9*, 11509−11539.
(29) Mak, K. F.; Lee, C.; Hone, J.; Shan, J.; Heinz, T. F. Atomically Thin MoS 2: a New Direct-Gap Semiconductor. *Phys. Rev. Lett.* **2010**, *105*, 136805.
(30) Wang, Q. H.; Kalantar-Zadeh, K.; Kis, A.; Coleman, J. N.; Strano, M. S. Electronics and Optoelectronics of Two-Dimensional Transition Metal Dichalcogenides. *Nat. Nanotechnol.* **2012**, *7*, 699.
(31) Zeng, H.; Dai, J.; Yao, W.; Xiao, D.; Cui, X. Valley Polarization in MoS 2 Monolayers by Optical Pumping. *Nat. Nanotechnol.* **2012**, *7*, 490.
(32) Xiao, D.; Liu, G. B.; Feng, W.; Xu, X.; Yao, W. Coupled Spin and Valley Physics in Monolayers of MoS2 and Other Group-VI Dichalcogenides. *Phys. Rev. Lett.* **2012**, *108*, 196802 DOI: 10.1103/PhysRevLett.108.196802.
(33) Kioseoglou, G.; Hanbicki, A.; Currie, M.; Friedman, A.; Gunlycke, D.; Jonker, B. Valley Polarization and Intervalley Scattering in Monolayer MoS2. *Appl. Phys. Lett.* **2012**, *101*, 221907.
(34) Enachescu, M.; Schleef, D.; Ogletree, D. F.; Salmeron, M. Integration of PointContact Microscopy and Atomic-Force Microscopy: Application to Characterization of Graphite/Pt(111). *Phys. Rev. B: Condens. Matter Mater. Phys.* **1999**, *60*, 16913−16919.
(35) Kim, H.; Hasegawa, Y. Insensitivity of Atomic Point Contact Conductance to a Moiré Structure. *Phys. Rev. B: Condens. Matter Mater. Phys.* **2016**, *93*, No. e075409.
(36) Bampoulis, P.; Sotthewes, K.; Siekman, M. H.; Zandvliet, H. J. W. Local Conduction in $Mo_xW_{1-x}Se_2$: The Role of Stacking Faults, Defects, and Alloying. *ACS Appl. Mater. Interfaces* **2018**, *10*, 13218.
(37) Celano, U.; Hantschel, T.; Giammaria, G.; Chintala, R. C.; Conard, T.; Bender, H.; Vandervorst, W. Evaluation of the Electrical Contact Area in Contact-Mode Scanning Probe Microscopy. *J. Appl. Phys.* **2015**, *117*, 214305.
(38) Peto, J.; Ollár, T.; Vancsó, P.; Popov, Z. I.; Magda, G. Z.; Dobrik, G.; Hwang, C.; Sorokin, P. B.; Tapasztó, L. Spontaneous Doping of the Basal Plane of MoS_2 Single Layers through Oxygen Substitution under Ambient Conditions. *Nat. Chem.* **2018**, *10*, 1246.
(39) Addou, R.; McDonnell, S.; Barrera, D.; Guo, Z.; Azcatl, A.; Wang, J.; Zhu, H.; Hinkle, C. L.; Quevedo-Lopez, M.; Alshareef, H. N.; et al. Impurities and Electronic Property Variations of Natural MoS_2 Crystal Surfaces. *ACS Nano* **2015**, *9*, 9124−9133.
(40) Addou, R.; Colombo, L.; Wallace, R. M. Surface Defects on Natural MoS_2. *ACS Appl. Mater. Interfaces* **2015**, *7*, 11921−11929.
(41) Liu, H.; Chen, J.; Yu, H.; Yang, F.; Jiao, L.; Liu, G.-B.; Ho, W.; Gao, C.; Jia, J.; Yao, W.; et al. Observation of Intervalley Quantum Interference in Epitaxial Monolayer Tungsten Diselenide. *Nat. Commun.* **2015**, *6*, 8180.
(42) Yankowitz, M.; McKenzie, D.; LeRoy, B. J. Local Spectroscopic Characterization of Spin and Layer Polarization in WSe 2. *Phys. Rev. Lett.* **2015**, *115*, 136803.
(43) Barja, S.; Refaely-Abramson, S.; Schuler, B.; Qiu, D. Y.; Pulkin, A.; Wickenburg, S.; Ryu, H.; Ugeda, M. M.; Kastl, C.; Chen, C., et al.. Identifying Substitutional Oxygen as a Prolic Point Defect in Monolayer Transition Metal Dichalcogenides with Experiment and Theory. 2018, arXiv:1810.03364. arXiv.org e-Print archive. https://arxiv.org/abs/1810.03364, accessed October 8, 2018.
(44) Chen, L.; Cheng, P.; Wu, K. Quasiparticle Interference in Unconventional 2D Systems. *J. Phys.: Condens. Matter* **2017**, *29*, 103001.
(45) Kaasbjerg, K.; Martiny, J. H.; Low, T.; Jauho, A.-P. Symmetry-Forbidden Intervalley Scattering by Atomic Defects in Monolayer Transition-Metal Dichalcogenides. *Phys. Rev. B: Condens. Matter Mater. Phys.* **2017**, *96*, 241411.
(46) Absor, M. A. U.; Kotaka, H.; Ishii, F.; Saito, M. Strain-Controlled Spin Splitting in the Conduction Band of Monolayer WS 2. *Phys. Rev. B: Condens. Matter Mater. Phys.* **2016**, *94*, 115131.
(47) Silva-Guillén, J. Á.; San-Jose, P.; Roldán, R. Electronic Band Structure of Transition Metal Dichalcogenides from Ab Initio and Slater−Koster Tight-Binding Model. *Appl. Sci.* **2016**, *6*, 284.
(48) Bampoulis, P.; Van Bremen, R.; Yao, Q.; Poelsema, B.; Zandvliet, H. J.; Sotthewes, K. Defect Dominated Charge Transport and Fermi Level Pinning in MoS_2/Metal Contacts. *ACS Appl. Mater. Interfaces* **2017**, *9*, 19278−19286.
(49) Derjaguin, B. V.; Muller, V. M.; Toporov, Y. P. Effect of Contact Deformations on the Adhesion of Particles. *J. Colloid Interface Sci.* **1975**, *53*, 314−326.
(50) Carpick, R. W.; Ogletree, D. F.; Salmeron, M. A General Equation for Fitting Contact Area and Friction vs Load Measurements. *J. Colloid Interface Sci.* **1999**, *211*, 395−400.
(51) Cappella, B.; Dietler, G. Force-Distance Curves by Atomic Force Microscopy. *Surf. Sci. Rep.* **1999**, *34*, 1−104.
(52) Frammelsberger, W.; Benstetter, G.; Kiely, J.; Stamp, R. C-AFM-Based Thickness Determination of Thin and Ultra-Thin SiO_2 Films by Use of Different Conductive-Coated Probe Tips. *Appl. Surf. Sci.* **2007**, *253*, 3615−3626.
(53) Bampoulis, P.; Teernstra, V. J.; Lohse, D.; Zandvliet, H. J. W.; Poelsema, B. Hydrophobic Ice Conned between Graphene and MoS_2. *J. Phys. Chem. C* **2016**, *120*, 27079−27084.

DOI: 10.1021/acs.nanolett.8b04636
Nano Lett. XXXX, XXX, XXX−XXX